Broadband Mode Coupling with Record-High Fabrication Tolerance Using the Stimulated Raman Adiabatic Passage Technique

Yingdi Pan, Lu Sun, Kaile Chen, Xingfeng Li, Xiong Ni, Pan Hu, Songyue Liu, Qi Lu, Xintao He, Jianwen Dong,* and Yikai Su**

Coupled-waveguide structures are fundamental in photonic integrated circuits for their wide applications in basic optical functions such as directional coupling, polarization handling, and mode manipulation. However, the couplings between waveguides usually suffer from high wavelength and structure sensitivity, which hinders the development of broadband and fabrication-tolerant devices. Here, a new method based on the stimulated Raman adiabatic passage (STIRAP) procedure is proposed for various kinds of on-chip mode manipulation such as mode conversion and multiplexing. The coupling process of the STIRAP system is thoroughly explored to reveal the topological nature of STIRAP. The experimental results prove that the mode-division multiplexer employing the STIRAP scheme has low insertion losses of < 1.8 dB and intermodal crosstalk of < −17.3 dB for all four mode channels over a 100-nm wavelength range (1480–1580 nm). Thanks to the topological protection of the mode coupling, the proposed multiplexer exhibits unprecedented fabrication tolerance (−80–100 nm) to the structural deviations in waveguide width and gap distance. This work provides an intriguing approach to expanding the working bandwidth and improving the fabrication tolerance of coupled-waveguide devices, which may find applications in diverse fields including optical communications, optical computing, quantum information processing and beyond.

1. Introduction

Coupled-waveguide devices are of central importance in photonic integrated circuits for their wide applications in optical functions such as directional coupling,[1] polarization beam splitting and rotation,[2] mode conversion and multiplexing,[3,4] etc. However, the couplings between different waveguides and modes usually suffer from high wavelength and structure sensitivity, which makes it challenging to achieve broadband and fabrication-tolerant devices. High fabrication precision is crucial for the device performance, which hinders the development of large-scale photonic integration and high-yield massive production. Great efforts have been devoted to address these issues, e. g., compensation via Mach–Zehnder interferometers,[5] robust coupling enabled by adiabatic evolution designs,[6] and dispersion engineering in subwavelength grating structures.[7–9] Nonetheless, there is still a high demand for wavelength- and structure-insensitive devices with naturally robust coupling mechanisms. Recently, topological photonics has emerged as a promising solution to broadening the working bandwidth and enhancing the fabrication tolerance of coupled-waveguide devices. For example, robust directional coupling and beam splitting were first demonstrated in Su–Schrieffer–Heeger (SSH) modeled waveguide arrays.[10] Then the Thouless pumping mechanism was exploited to realize robust power coupling and mode-order conversions in Rice–Mele (RM) modeled waveguide arrays.[11] These works suggest that topological photonics offers unprecedented opportunities for realizing robust photonic integration.

Stimulated Raman adiabatic passage (STIRAP) technique, first proposed in 1990 to produce efficient population transfer between two rovibrational energy levels of molecules,[12] has found widespread applications in many fields of physics, chemistry, and information processing within the last 35 years.[13] In integrated photonics, it can be mimicked by a coupled-waveguide structure with spatially varying coupling strengths.[14–18] Although the STIRAP process has long been known to have high tolerance to system parameter variations, the topological aspect of the underlying mechanism remains elusive. Recently, the STIRAP technique was used to realize broadband mode converters.[19]

Y. Pan, L. Sun, K. Chen, X. Li, X. Ni, P. Hu, S. Liu, Q. Lu, Y. Su
State Key Laboratory of Advanced Optical Communication Systems and Networks
Department of Electronic Engineering
Shanghai Jiao Tong University
Shanghai 200240, China
E-mail: sunlu@sjtu.edu.cn; yikaisu@sjtu.edu.cn
X. He, J. Dong
State Key Laboratory of Optoelectronic Materials and Technologies
School of Physics
Sun Yat-Sen University
Guangzhou 510275, China
E-mail: dongjwen@mail.sysu.edu.cn

The ORCID identification number(s) for the author(s) of this article can be found under https://doi.org/10.1002/lpor.202401756

DOI: 10.1002/lpor.202401756

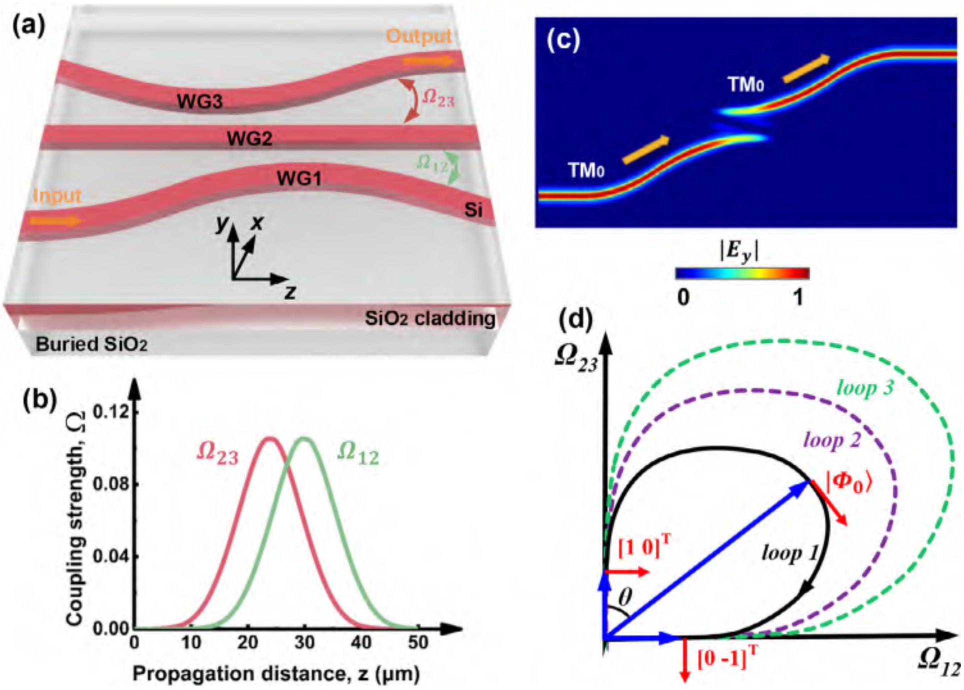

Figure 1. STIRAP process realized by coupled waveguides. a) 3D schematic of the coupled-waveguide structure that mimics the STIRAP process. b) Evolution of the coupling strengths Ω_{12} and Ω_{23} along the propagation direction z. c) Light propagation profile ($|E_y|$) of the TM_0 mode in the three-waveguide structure in a. d) Evolutionary trajectory of the coupling strengths in the $(\Omega_{12}, \Omega_{23})$-space and the transport of the state vector $|\Phi_0\rangle$ along the trajectory.

However, the mechanism behind the wavelength insensitivity was not clearly explained and how the mechanism can be exploited to enhance the fabrication tolerance of the mode handling devices was not discussed. Here, we first reveal the topological nature of the STIRAP scheme and find the topological invariant related to the robust mode coupling between waveguides. Then we utilize the topological protection provided by the STIRAP scheme to realize broadband and fabrication-tolerant on-chip mode manipulation. As compared to most of the topological coupled waveguides reported previously,[10,20] the structure based on the STIRAP technique is more advantageous because it shows greater robustness against the variations in not only wavelength and gap but also waveguide width. To characterize the insertion loss (IL) and intermodal crosstalk (CT) of the mode coupling processes, various mode-order converters employing the STIRAP scheme are cascaded to form a four-channel mode-division multiplexer (MDM). The experimental results prove that the proposed multiplexer exhibits low ILs of < 1.8 dB and CT values of < -17.3 dB over a 100-nm bandwidth (1480–1580 nm) for all the four mode channels. Structural parameter discrepancies were also intentionally introduced to the STIRAP structure and its conventional counterpart based on asymmetric directional couplers (ADCs). Thanks to the topological nature of the STIRAP process, our design shows unprecedented fabrication tolerance (−80–100 nm) for the structural deviations in waveguide width and gap distance while the performance of the conventional device deteriorates rapidly with increasing structural parameter errors. To the best of our knowledge, the proposed device has the highest fabrication tolerance among the coupled-waveguide mode-handling devices reported so far. Moreover, we performed a transmission experiment of four-level pulse amplitude modulation (PAM-4) signals to verify the capability of the topological devices in high-speed data transmission applications. The transmission capacity per lane reaches net 127 Gbit s^{-1}, with the bit error rates (BERs) below the 7% forward error correction (FEC) threshold of 3.8×10^{-3}. Our findings may pave a new way toward expanding the working bandwidth and loosening the fabrication precision requirement for coupled-waveguide devices, which would find wide applications in a variety of fields including high-capacity optical communications,[21,22] large-scale optical computing,[23,24] and high-fidelity quantum information processing.[25–27]

2. Results

2.1. STIRAP Revisited: The Topological Nature of STIRAP

Figure 1a shows the 3D schematic of the coupled-waveguide structure that mimics the STIRAP process. The light is input from the lower waveguide (WG1), mediated by the central waveguide (WG2) and output from the upper waveguide (WG3). The coupling Ω_{23} between WG2 and WG3 precedes the coupling Ω_{12} between WG1 and WG2 in the propagation direction z, as illustrated in Figure 1b. The counterintuitive order of couplings is a unique feature of STIRAP and plays a key role in the robust excitation transfer. When the light is initially launched from WG1, it excites only the dark state of the system that does not involve WG2. As one can see from Figure 1c, the light transmits from WG1 to WG3 without any light in WG2, even transiently. Therefore, the properties of WG2, including possible losses and detuning of mode effective index with respect to WG1 and WG3, are largely irrelevant to the system performance, which leads to the robustness against the waveguide width variation. Using the coupled mode theory, the analytical expression of the dark state $|\Phi_0\rangle$ can be written as:[13–15,17]

$$|\Phi_0\rangle = \frac{\Omega_{23}}{\sqrt{\Omega_{12}^2 + \Omega_{23}^2}} |\psi_1\rangle - \frac{\Omega_{12}}{\sqrt{\Omega_{12}^2 + \Omega_{23}^2}} |\psi_3\rangle \tag{1}$$

where $|\psi_1\rangle$ and $|\psi_3\rangle$ are the wave functions of the eigen states in WG1 and WG3, respectively. In other words, $|\Phi_0\rangle$ can be expressed by a vector $[\,\frac{\Omega_{23}}{\sqrt{\Omega_{12}^2+\Omega_{23}^2}}\ \ \frac{-\Omega_{12}}{\sqrt{\Omega_{12}^2+\Omega_{23}^2}}\,]^{\mathrm{T}}$ in the subspace spanned by $|\psi_1\rangle$ and $|\psi_3\rangle$ (Section S1, Supporting Information). In Figure 1d, we display the evolution of the coupling strengths between waveguides in the $(\Omega_{12}, \Omega_{23})$-space and the transport of the dark state along the evolutionary trajectory. As the propagation distance increases, the coupling coefficients of the system in Figure 1c evolve along a closed path clockwise (loop 1 in Figure 1d with the evolutionary direction indicated by the black arrow) in the parameter space spanned by Ω_{12} and Ω_{23}. We find that the vector $[\,\Omega_{12}\ \ \Omega_{23}\,]^{\mathrm{T}}$ in the parameter space (represented by the blue arrows in Figure 1d) is always orthogonal to the vector $|\Phi_0\rangle$ in the state space (represented by the red arrows in Figure 1d). In the language of topology, the state space forms a vector bundle on the closed loop in the parameter manifold.[28] For the state vector to evolve from $[\,1\ 0\,]^{\mathrm{T}}$ to $[\,0\ -1\,]^{\mathrm{T}}$ (i. e., the light is coupled from WG1 to WG3), the parameter vector should change from aligning with the vertical axis to aligning with the horizontal axis in the $(\Omega_{12}, \Omega_{23})$-space. Most importantly, the variations in wavelength and gap distance between waveguides will cause the deformations of the parametric loop, e. g., loop 1 becomes loop 2 or loop 3 in Figure 1d. However, the deformations do not change the fact that the parameter vector and the state vector rotate clockwise by 90° during the coupling processes, which is the key to producing a complete power transfer between WG1 and WG3. The phenomenon can be described by a topological invariant θ defined as:

$$\theta = \oint_{loop} d\arctan\frac{\Omega_{12}}{\Omega_{23}} = \int_0^L \frac{\Omega'_{12}\Omega_{23} - \Omega_{12}\Omega'_{23}}{\Omega_{12}^2 + \Omega_{23}^2} dz \tag{2}$$

where θ corresponds to the angle between the parameter vector and the vertical axis (see Figure 1d), L is the coupling length in the z direction, and Ω'_{12} and Ω'_{23} are the first-order derivatives of the coupling strengths with respect to the propagation distance z. For a complete excitation transfer, $\theta = \frac{\pi}{2}$ and it remains invariant under some continuous changes of the parametric loop. Therefore, this is a topological property of the STIRAP procedure that is robust to the variations in system design parameters such as wavelength and gap distance between waveguides (the coupling strengths between waveguides depend strongly on these parameters). We would like to point out that the counterintuitive order of couplings in the STIRAP procedure could also be interpreted as a topological pumping scheme in the off-diagonal Aubre–Andre–Harper (AAH) model, which again verifies the topological origin of STIRAP.[29]

2.2. Topological Design of Mode Coupling Devices Based on the STIRAP Process

To prove the robust mode couplings enabled by the STIRAP mechanism, we first investigate various mode-order conversions in the evanescently coupled waveguides shown in **Figure 2a**. The structure can be routinely fabricated on the silicon-on-insulator (SOI) platform (3-μm-thick buried oxide layer, 220-nm-thick silicon top layer, and 1-μm-thick silica upper cladding layer) using current complementary metal-oxide semiconductor (CMOS)-compatible nanofabrication technologies.[30,31] We focus on the transverse magnetic (TM) modes hereafter since they have stronger coupling strengths and thus shorter coupling lengths. The width of WG1 W_1 is designed to be 420 nm to support only the TM_0 mode. To meet the phase matching condition between the fundamental mode in WG1 and the high-order modes in WG3, we use the commercial eigenmode solver (Lumerical MODE Solutions) to calculate the mode effective indices and choose different widths of WG3 W_3 for the TM_1-TM_3 modes, as listed in **Table 1**. As we have already mentioned, the width of WG2 W_2 has little influence on the performance of the STIRAP system due to the fact that the mode coupling depends only on the dark state. However, the presence of WG2 is essential, which means WG2 cannot be removed from the system (Section S2, Supporting Information). Here we set W_2 to be 420 nm to ensure strong couplings with WG1 and WG3. WG1 and WG3 are curved to couple with WG2 in an adiabatic way (the bending radius of the curve is larger than 250 μm) so that only the dark state is involved during the evolution of STIRAP. The coupling lengths L are designed to be 54, 63, and 69 μm for the TM_0-to-TM_1, TM_0-to-TM_2, and TM_0-to-TM_3 mode conversions, respectively (Section S3, Supporting Information). Along the propagation direction, WG2 is first coupled to WG1 before it is coupled to WG3, accomplishing the counterintuitive order of couplings in the STIRAP process. The minimum gap between WG1 and WG2 is g_{12} and that between WG2 and WG3 is g_{23}. The distance in the z direction between the positions with minimum gaps is denoted as d, as schematically illustrated in Figure 2a. With proper design parameters shown in Table 1, one can realize different mode-order conversions with high efficiencies and robustness based on the STIRAP structures. More details of the design method can be found in Section S3 (Supporting Information). It is noteworthy that the minimum feature size of our design is 100 nm, which is not compatible with the fabrication process of some foundries. Another design example with improved foundry compatibility (a minimum feature size of 130 nm) is provided in Section S4 (Supporting Information).

The full-wave numerical simulations of the mode-order conversions were performed using the 3D finite-difference time-domain (3D FDTD) methods. Figure 2b–d displays the simulated electric field distributions ($|E_y|$) in the coupling regions for the TM_0-to-TM_1, TM_0-to-TM_2, and TM_0-to-TM_3 mode conversions, respectively. Obviously, the TM_0 mode launched from WG1 is efficiently converted to the $TM_{1,2,3}$ mode in WG3 with almost no excitation in WG2. The mode overlapping constants between the output fields and the eigen mode fields are calculated to evaluate the IL and CT levels (Section S3, Supporting Information). Figure 2e–g presents the simulated transmission spectra

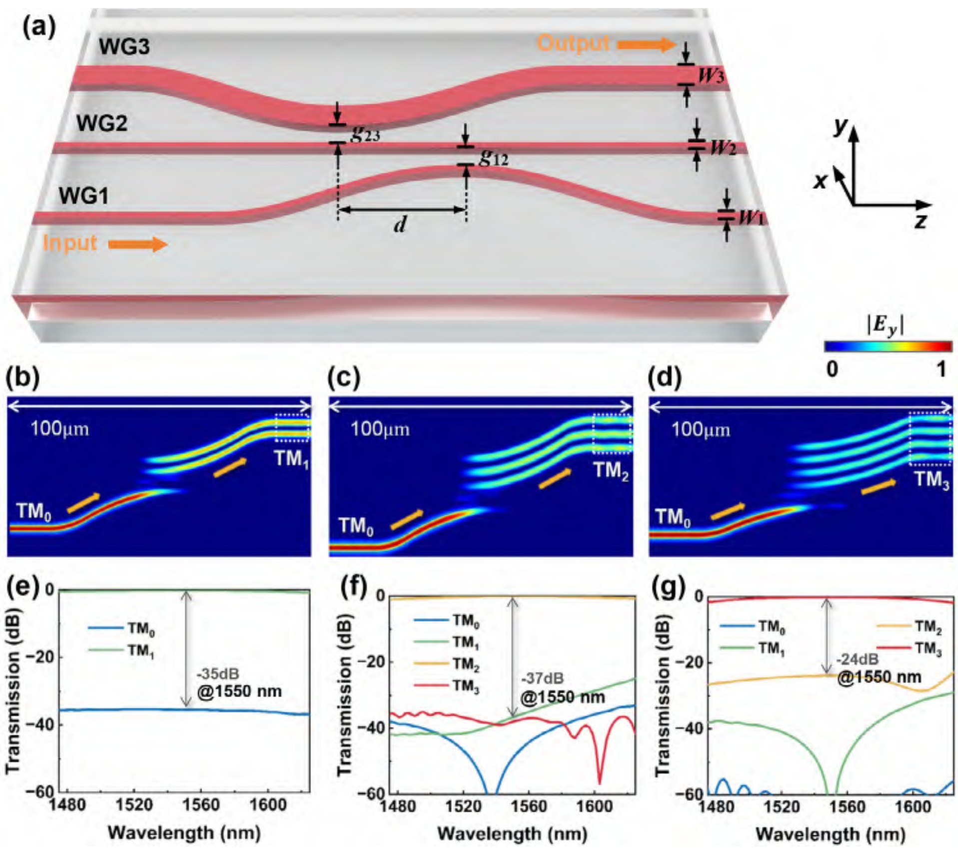

Figure 2. Mode-order conversions based on the STIRAP mechanism. a) 3D schematic of the STIRAP structure for different mode-order conversions. b–d) Light propagation profiles ($|E_y|$) at 1550 nm for the b) TM_0-to-TM_1, c) TM_0-to-TM_2, and d) TM_0-to-TM_3 mode conversions when the TM_0 mode is launched from WG1. e–g) Simulated transmission spectra of different modes output from WG3 of the e) TM_0-to-TM_1, f) TM_0-to-TM_2, and g) TM_0-to-TM_3 mode coupling regions in b–d.

Table 1. Design parameters for different mode-order conversions.

Mode-order conversion	W_1 [nm]	W_2 [nm]	W_3 [nm]	g_{12} [nm]	g_{23} [nm]	d [μm]	L [μm]
TM_0-to-TM_1	420	420	1060	130	130	9	54
TM_0-to-TM_2	420	420	1740	110	110	11	63
TM_0-to-TM_3	420	420	2400	200	100	12	69

of different modes for the mode-order conversions shown in Figure 2b–d. In the wavelength range of 1475–1625 nm which covers the C- and L-band, the ILs are less than 0.75, 0.70, and 1.59 dB and the CT values are below −35.0, −25.6, and −24.0 dB for the TM_0-to-TM_1, TM_0-to-TM_2, and TM_0-to-TM_3 conversions, respectively (all below −24 dB at 1550 nm). The 1-dB IL bandwidth is larger than 120 nm (1488–1608 nm) for all the mode-order conversions, proving the broadband property of the mode couplings between waveguides employing the STIRAP mechanism.

To prove the robustness of the topological design against the structural parameter variations, we compare the mode-order conversions based on the STIRAP structure with their conventional counterparts based on ADCs. The ADCs consist of a single-mode waveguide with a width of W_1 and a multimode waveguide with a width of W_3. The coupling lengths are fixed at 100 μm. Although by reducing the gaps one can achieve shorter coupling lengths and broader bandwidths, the fabrication tolerance of such ADCs is usually within ±10 nm.[10,11] In comparison, the ADCs with large gaps and long coupling lengths are more tolerant to the variations in gap distance and waveguide width. To investigate the fabrication tolerance of the topological and conventional designs, gap distance deviations and waveguide width deviations are intentionally introduced to both coupled-waveguide structures. The gap distance deviations are Δg for all the gaps between waveguides while the waveguide width deviations are Δw for WG1 and WG2, and $1.7\Delta w$, $2.3\Delta w$, and $3.1\Delta w$ for WG3 in the TM_0-to-TM_1, TM_0-to-TM_2, and TM_0-to-TM_3 conversions, respectively. The waveguide width deviations are assumed to be larger for WG3 than those for WG1 to meet the phase matching condition between the fundamental mode in WG1 and the high-order modes in WG3 required by the STIRAP process. In contrast, the waveguide width deviations of WG2 are irrelevant to the system performance (they do not have to be Δw) because WG2 is actually not involved in the STIRAP evolution. **Figure 3a–f** shows the simulated transmission of the target modes (TM_1-TM_3) at 1550 nm as functions of waveguide width deviation Δw (Figure 3a–c) and gap distance deviation

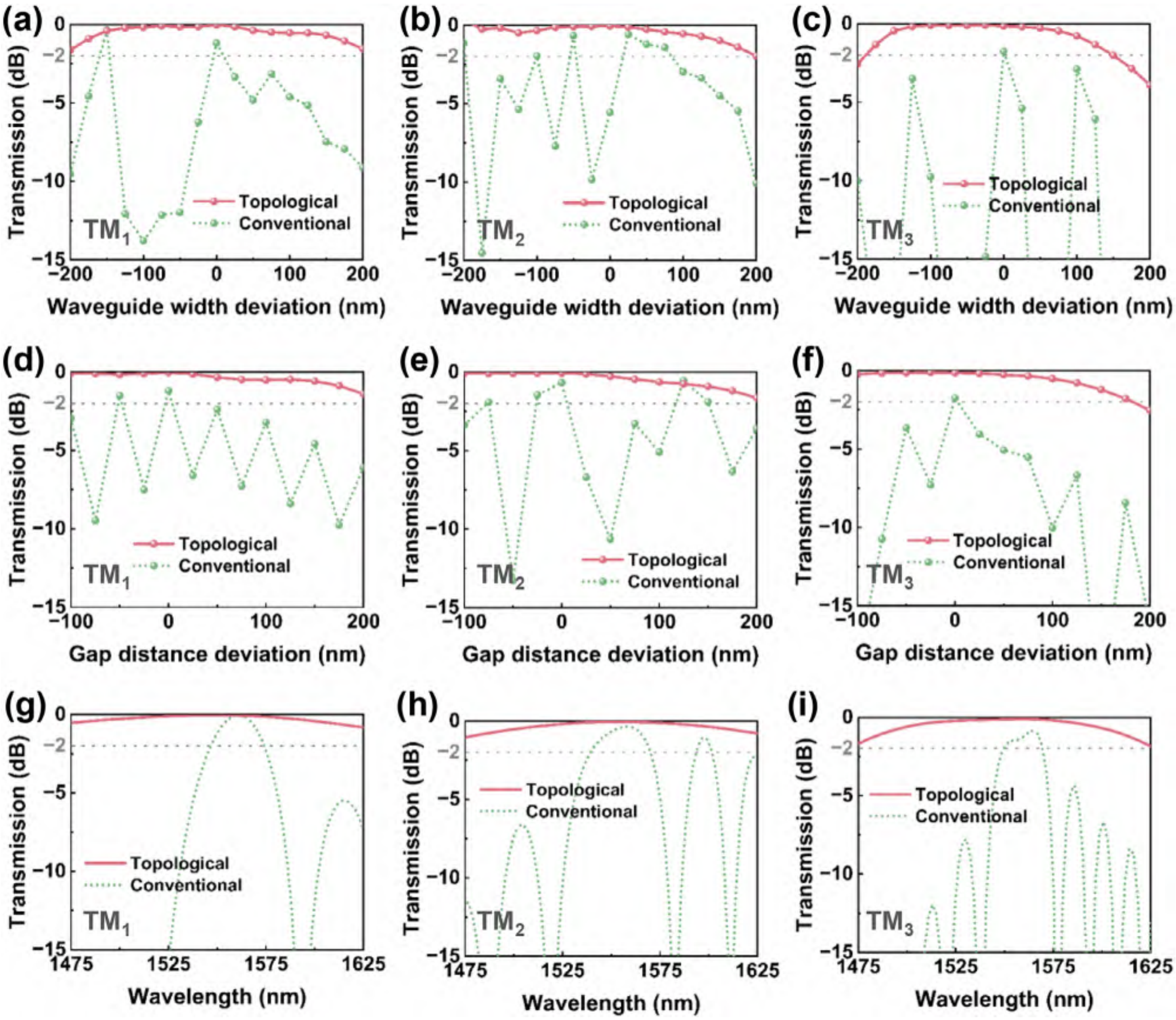

Figure 3. Comparison of the topological and conventional mode-order conversions. a–f) Simulated transmission of the target modes at 1550 nm when a–c) the waveguide width deviation Δw varies from −200 to 200 nm or d–f) the gap distance deviation Δg varies from −100 to 200 nm. g–i) Simulated transmission spectra of the target modes for different mode-order converters. The left, middle and right columns of figures correspond to the TM_0-to-TM_1, TM_0-to-TM_2 and TM_0-to-TM_3 conversions, respectively.

Δg (Figure 3d–f). Over a wide range of structural parameter discrepancies (−150–150 nm for Δw and −100–175 nm for Δg), the ILs of the topological devices are maintained below 2 dB while those of the conventional devices degrade significantly with increasing deviations. The comparison shows clear evidence that the mode couplings following the STIRAP procedure are topologically protected and therefore much more tolerant to the structural deviations in both waveguide width and gap distance. It is worth mentioning that in reality the gaps are more likely to shrink by the same amount as the waveguides widen and vice versa, so we also investigate the fabrication tolerance of both the topological and conventional devices under the circumstances that the waveguides keep a fixed center-to-center distance and get narrower or wider by the same amount (Section S5, Supporting Information). Figure 3g–i presents the simulated transmission spectra of the target modes for both the topological and conventional mode-order converters. Owing to the broadband nature of the mode couplings, the topological devices exhibit low ILs of < 2 dB over a 150-nm bandwidth ranging from 1475 to 1625 nm, covering the C- and L-band. In comparison, the 2-dB IL bandwidths of the conventional devices are less than 30 nm, which are more than 5 times narrower than their topological counterparts. It is obvious that the topological designs possess better robustness against the wavelength variation compared to the conventional ones, which is beneficial for achieving broadband mode coupling devices.

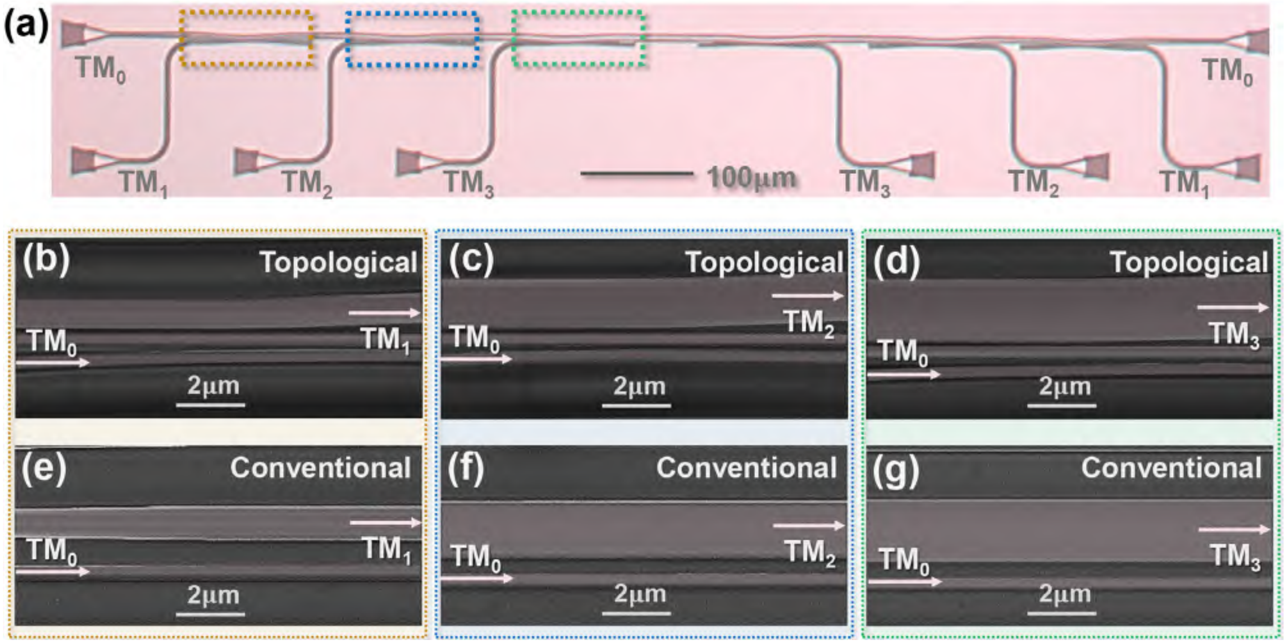

Figure 4. Structures of the fabricated four-channel MDMs. a) Optical microscope image of the fabricated MDM based on STIRAP. The correspondence between the ports and the modes is indicated in the figure. The TM_0-to-TM_1, TM_0-to-TM_2 and TM_0-to-TM_3 mode conversion regions are encircled by the yellow, blue, and green dashed boxes, respectively. b–d) SEM images of the coupled waveguides in the topological device for the b) TM_0-to-TM_1, c) TM_0-to-TM_2 and d) TM_0-to-TM_3 conversions. e–g) SEM images of the coupled waveguides in the conventional device for the e) TM_0-to-TM_1, f) TM_0-to-TM_2 and g) TM_0-to-TM_3 conversions.

2.3. Experimental Results

To characterize the ILs and the intermodal CT of the mode coupling processes discussed in Section 2.2, we cascaded the topological and conventional mode-order converters to form two kinds of four-channel MDMs, as shown in **Figure 4**. Different mode-order converters were connected through WG3 using the adiabatically tapered waveguides. The topological and conventional multiplexers were fabricated on a SOI wafer (220-nm-thick silicon layer on top of 3-μm-thick buried oxide layer) with CMOS-compatible fabrication processes.[30,31] The fabrication procedure is detailed in Section 4. The device structures were patterned using electron beam lithography (EBL) and etched by inductively coupled plasma (ICP) dry etching. A 1-μm-thick silica upper cladding layer was then deposited over the devices by plasma enhanced chemical vapor deposition (PECVD). Figure 4a shows the optical microscope image of the fabricated device employing the STIRAP protocol. Figure 4b–d displays the scanning electron microscope (SEM) images of the coupled waveguides in the TM_0-to-TM_1, TM_0-to-TM_2 and TM_0-to-TM_3 mode conversion regions of the topological design while Figure 4e–g presents those of the conventional ADCs.

In the transmission measurement, a tunable continuous wave (CW) laser and a photodetector (PD) were employed to obtain the transmission spectra of the fabricated devices. Grating couplers (GCs) were used to couple the TM-polarized light into and out of the chip. The coupling losses of the GCs were ≈6 dB/facet at the central wavelength of 1550 nm. The transmission spectra of the devices were normalized to that of the reference GCs fabricated on the same chip. More details about the experimental setup and the measurement methods can be found in Section 4. In **Figure 5**, we present the measured spectral responses of the topological MDM using the STIRAP technique. The light was injected from the TM_0-TM_3 ports on the left side of the device to realize the four-mode multiplexing in the bus waveguide. After propagating in the bus waveguide for a distance, the modes were then demultiplexed using the same coupled-waveguide structures based on STIRAP and output from the corresponding ports on the right side of the device. Thanks to the broadband nature of the topological design, the measured ILs of the TM_0-TM_3 mode channels are lower than 0.4, 1.3, 1.7, and 1.8 dB respectively, over a 100-nm bandwidth of 1480–1580 nm. It means that the measured ILs of the TM_0-to-$TM_{1,2,3}$ mode-order converters are less than 0.65, 0.85, and 0.9 dB respectively, which are in good agreement with the simulation results shown in Figure 2e–g. The ILs could be attributed to the bending losses, the energy leakage through WG1 and WG2, the scattering losses caused by the waveguide sidewall roughness and the imperfect couplings due to the partial filling of the gaps with the cladding material.[32] They can be further reduced by optimizing the design and fabrication process. The measured CT values are below −18.7, −17.3, −18.2, and −20.0 dB in the same wavelength range for the TM_0-TM_3 mode channels, respectively (all below −20 dB at 1550 nm). As a comparison, the measured 3-dB IL bandwidth of the conventional MDM based on ADCs is only ≈10 nm and the CT is less than −10 dB over the entire 100-nm bandwidth (Section S7, Supporting Information). It is evident that the topological design based on STIRAP significantly relieves the wavelength sensitivity of the mode coupling devices.

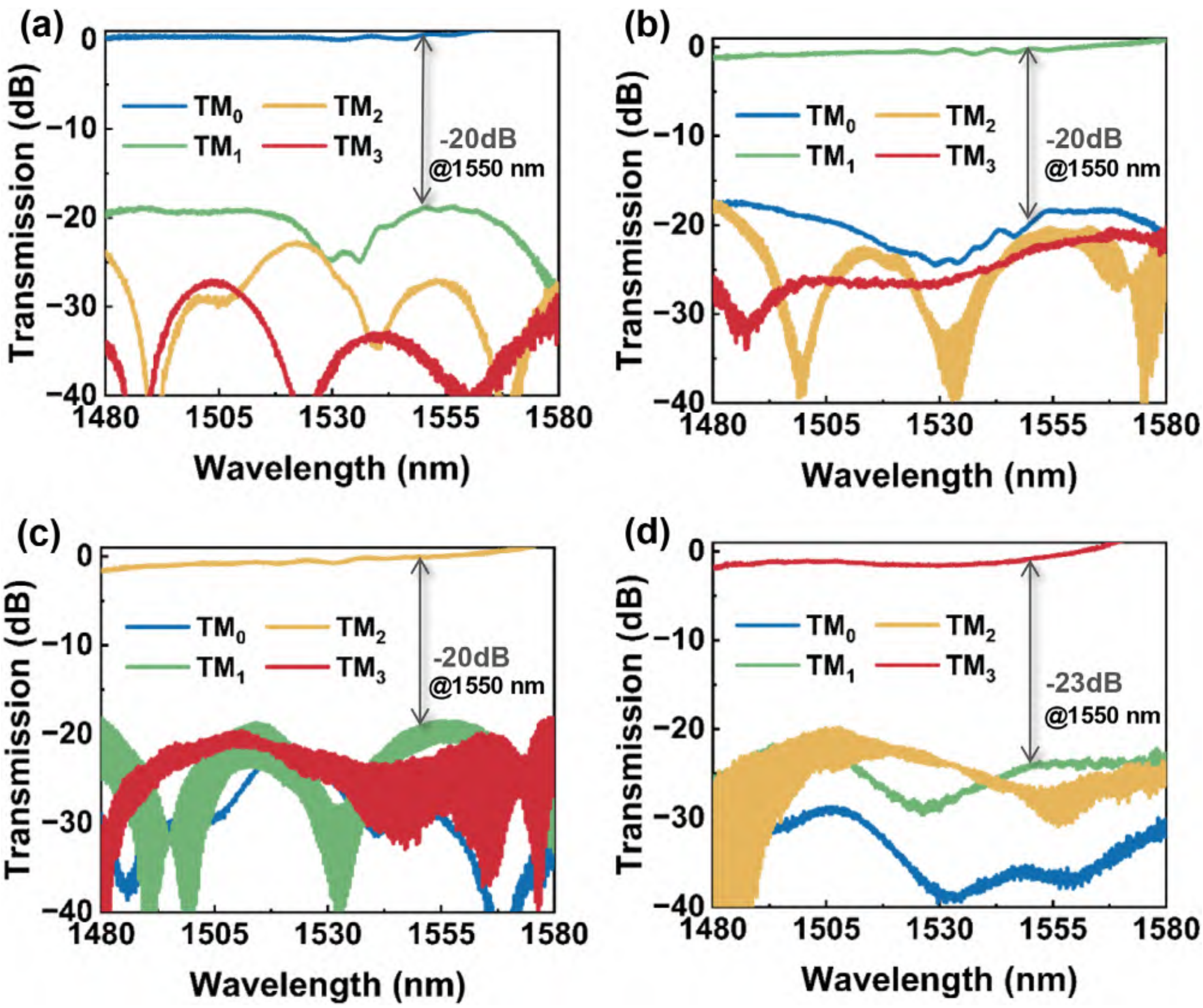

Figure 5. Measured transmission spectra of the TM_0-TM_3 modes when the light is respectively input from the a) TM_0, b) TM_1, c) TM_2 and d) TM_3 ports on the left side of the proposed MDM.

To compare the fabrication tolerance of the topological and conventional MDMs, we also fabricated a series of controlled samples in which structural parameter discrepancies were deliberately introduced to the waveguide width and the gap distance of the coupled-waveguide structures. **Figure 6** shows the measured transmission of the target modes at 1550 nm for the topological and conventional devices with the waveguide width deviation Δw and the gap distance deviation Δg varied within a wide range. The measured ILs of the topological devices are lower than 3 dB even with large fabrication errors (−80–180 nm for the TM_1 mode, −100–140 nm for the TM_2 mode and −100–100 nm for the TM_3 mode). In contrast, the performance of the conventional devices deteriorates rapidly with the structural parameters deviating from the designed values. The discrepancies of ILs between the theory and the experiment could be attributed to the scattering losses caused by the waveguide sidewall roughness and the imperfect couplings due to the partial filling of the gaps with the cladding material. A reduction in fabrication tolerance can be observed with increasing mode order because the high-order modes are close to each other in mode effective index and therefore more sensitive to the structural parameter changes. Considering current nanofabrication technologies, two adjacent waveguides cannot be well separated at the positions where the gaps are smaller than 50 nm. Nonetheless, the experimental results clearly show that the topological design exhibits remarkable robustness to the structural deviations in waveguide width and gap distance (even if the waveguides are in contact with each other at the minimum gap point), which is highly desirable in large-scale photonic integration. It is worth mentioning that the topological design method based on the STIRAP scheme can also be applied to the mode couplings for the transverse electric (TE) polarization (Section S8, Supporting Information). Combining both the mode- and polarization-division multiplexing will further increase the number of channels and therefore scale the link capacity of the on-chip optical transmission system.

As a proof of its possible application, we conducted a transmission experiment based on the four-channel topological MDM by sending one high-Baud-rate signal to each channel at a time.

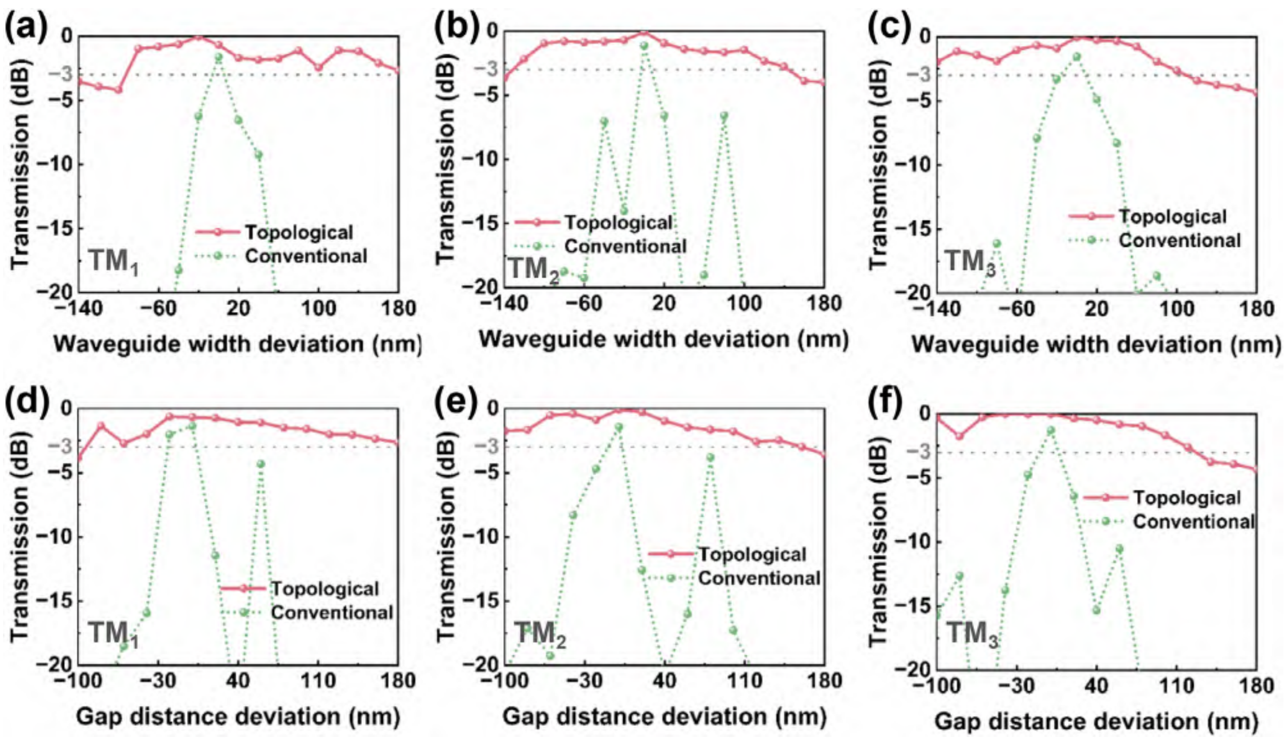

Figure 6. Measured transmission of the target modes at 1550 nm for the topological and conventional MDMs with various fabrication errors. a–c) Measured transmission of the a) TM_1, b) TM_2 and c) TM_3 modes when the waveguide width deviation Δw varies from −140 to 180 nm. d–f) Measured transmission of the d) TM_1, e) TM_2 and f) TM_3 modes when the gap distance deviation Δg varies from −100 to 180 nm.

The experimental setup and transceiver digital signal processing (DSP) algorithms are shown in **Figure** 7a,b, respectively. A Nyquist-shaped 70-GBaud PAM-4 signal is transmitted through each channel of the fabricated device. At the receiver, a feedforward equalizer (FFE), post-filter, and maximum-likelihood sequence decision (MLSD) are employed to compensate for the transmission impairments. More detailed information about the experimental setup and the DSP can be found in Section 4. The measured optical spectra of the 70-GBaud PAM-4 signals at different stages are shown in Figure 7c. Figure 7d shows the BER performance for the four mode channels, all below the 7% hard-decision-forward error correction (HD-FEC) threshold of 3.8×10^{-3}. Considering the 7% FEC overhead and the frame redundancy, the 70-GBaud PAM-4 signal per channel has a net data rate of 127 Gb s^{-1}. Note that the calculated BERs are well below the 7% FEC threshold, so the data rate can be further improved by increasing the data rate of the signal source and adding an optical bandpass filter (OBPF) after each erbium-doped fiber amplifier (EDFA) to filter out the amplified spontaneous emission (ASE) noises. The recovered eye diagrams of the PAM-4 signals for different modes are presented in Figure 7e, indicating a good signal quality for all the channels. The high-speed data transmission experiment unambiguously verifies the feasibility of the topological mode (de)multiplexers in practical on-chip optical communication systems.

In **Table** 2, we compare the proposed device with some recently reported four-channel MDMs based on various structures. Our design exhibits low ILs of < 1.8 dB and CT values of < −17.3 dB over a broad bandwidth of 100 nm, which is comparable to the state of the art of silicon-based four-channel MDMs. Thanks to the topological nature of the STIRAP process, the mode conversion and multiplexing show excellent robustness to the structural parameter deviations. To the best of our knowledge, the topological design has the highest fabrication tolerance (–80–100 nm) among different kinds of mode coupling devices reported so far, which is very much desired for robust on-chip mode manipulation and high-capacity optical communications with scalable MDMs.

3. Conclusion

In conclusion, we have proposed and experimentally demonstrated a new design method for realizing wavelength- and structure-insensitive mode couplings based on the coupled-waveguide structures that mimic the STIRAP process. We first revisited the STIRAP protocol from a topological perspective and revealed the topological nature and the topological invariant related to the process. Then the topological protection of STIRAP was exploited for broadband and fabrication tolerant on-chip mode manipulation. As compared to other topological approaches,[10,20,39,40] the STIRAP method used in this work shows great robustness to the variations in not only wavelength and gap distance but also waveguide width. Using the proposed design method, we realized various robust and high-efficiency mode-order converters and created a four-channel MDM based on them. The experimental results show that the measured ILs and CT values are lower than 1.8 and −17.3 dB respectively for all the mode channels (TM_0-TM_3) of the topological MDM, over

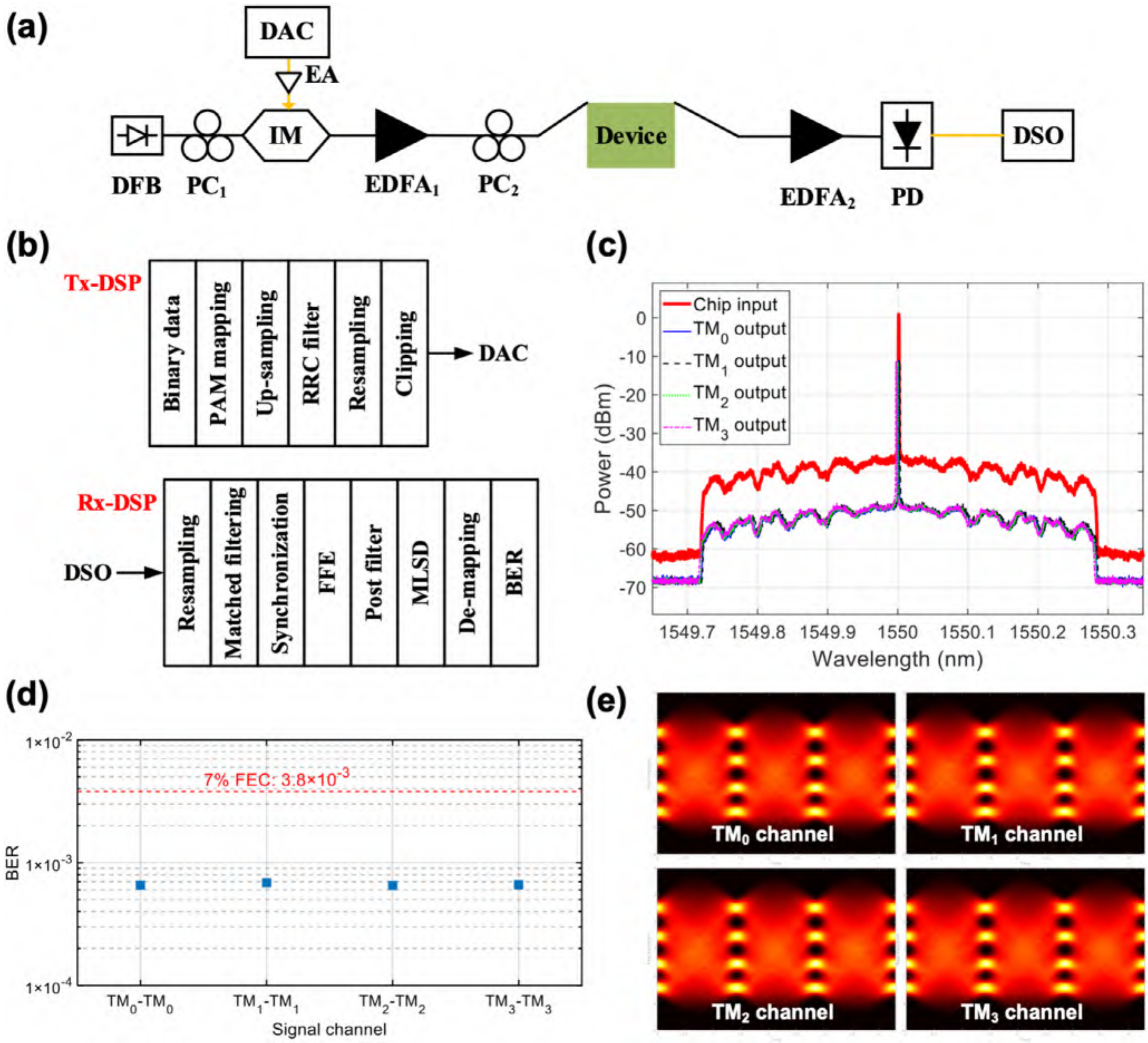

Figure 7. High-speed data transmission experiment based on the four-channel topological MDM. a) Experimental setup for the 127-Gb s^{-1} net-data-rate transmission experiment. The black and orange lines represent optical and electrical links, respectively. b) DSP algorithms for the transceivers. c) Measured optical spectra of the PAM-4 signals at different stages. d) BERs for the four signal channels. e) Recovered eye diagrams for each mode.

Table 2. Comparison of various silicon-based four-channel MDMs.

Refs	Structures	Bandwidth [nm]	IL [dB]	CT [dB]	Fabrication tolerance
[3]	ADCs	20	< 4	< −23	–
[33]	Coupled waveguides using shortcuts to adiabaticity	100	< 1.3	< −23	±20 nm
[34]	ADCs with subwavelength sidewall corrugations	50	< 4	< −16	±20 nm
[35]	Tilt waveguide junctions with shallow etched slots	60	< 1.29	< −14.4	–
[36]	Inverse-designed discretized meta-structures	60	< 3	< −14.6	±10 nm
[37]	Subwavelength grating-assisted triple-waveguide couplers	100	< 5	< −10	±20 nm
[38]	Tapered ADCs	75	< 6	< −16	±20 nm
This work	Triple waveguides based on STIRAP	100	< 1.8	< −17.3	−80–100 nm

a 100-nm wavelength range from 1480 to 1580 nm. Most importantly, the device is proved to be very robust to the structural deviations in waveguide width and gap distance (−80–100 nm), which is, to the best of our knowledge, the highest fabrication tolerance that has ever been reported in literature. All these merits are well confirmed in experiments by comparing with the conventional MDM based on ADCs, including controlled samples with intentionally introduced structural parameter discrepancies. Furthermore, high-speed transmission of PAM-4 signals has been successfully demonstrated based on the proposed MDM with a net data rate of 127 Gb s^{-1} per channel, which means the aggregate data rate would reach up to ≈508 Gb s^{-1} with all the four mode channels. It should be noted that the proposed design method based on STIRAP is universal and can be applied to various material platforms such as AlGaAs,[41] lithium niobate,[42,43] and silicon nitride (Section S9, Supporting Information). Future studies of this approach could be envisioned, for example, it can also be applied to the design of mode coupling devices for the TE polarization and perhaps more advanced multiplexing systems with higher-order modes and dual polarizations. Our work serves as a foundation for the development of a new class of broadband and fabrication tolerant coupled-waveguide devices, which would boost the progress in diverse areas ranging from optical communications to optical computing and quantum information processing.

4. Experimental Section

Sample Fabrication: The waveguides, GCs and four-channel MDMs were fabricated on a SOI wafer (220-nm-thick silicon layer on top of 3-μm-thick buried oxide layer). The wafer was first cleaned in ultrasound baths of acetone and isopropyl alcohol (IPA) and further cleaned using O_2 plasma asher. The patterns of the GCs were defined utilizing EBL (Vistec EBPG 5200$^+$). Then they were transferred onto the top silicon layer by ICP dry etching (SPTS DRIE-I) with an etching depth of 70 nm. The above steps were repeated to define the remaining structures such as waveguides and mode (de)multiplexers, but this time with an etching depth of 220 nm. After that, a 1-μm-thick silica upper cladding layer was deposited over the devices by PECVD (Oxford Plasmalab System 100). The fabricated samples were inspected using the optical microscope and the SEM (Zeiss Ultra Plus).

Optical Characterization: In the transmission measurement, the polarization of light from a tunable CW laser (Santec TSL-710) was first adjusted by a fiber polarization controller (PC). Then the TM-polarized light was coupled into and out of the chip by GCs. The coupling losses of the GCs were ≈6 dB/port at the central wavelength of 1550 nm. An optical power meter and a PD (Santec MPM-210) were used for optical calibration and receiving the transmitted power, respectively. The transmission spectra of the topological and conventional devices were normalized to that of the reference GCs. The ILs and CT values of the multiplexers were assessed based on the measurement. More details about the experimental setup and the measurement methods can be found in Section S6 (Supporting Information).

High-Speed Transmission: At the transmitter side, a 70-GBaud PAM-4 signal was generated by a digital-to-analog converter (DAC, Micram DAC4) with a sampling rate of 100 GSa s^{-1}. After being amplified by an electrical amplifier (EA), the electrical signals were used to drive an intensity modulator (IM) with a quadrature bias. A distributed feedback (DFB) laser was employed to output a 14-dBm continuous light, which was adjusted by a PC and then injected into the IM. After the electrical-to-optical (E/O) conversion, the generated optical PAM-4 signal was boosted by an EDFA and then coupled into the TM_0, TM_1, TM_2 and TM_3 mode channels of the proposed MDM, respectively. At the receiver side, the signal was amplified by an EDFA to compensate for the loss. Finally, the optical signal was detected with a 50-GHz PD and captured using a 80 GSa s^{-1} digital storage oscilloscope (DSO, LeCroy 59Zi-A). The receiver DSP consists of resampling, match-filtering, and synchronization. Then a least-mean-square (LMS) algorithm-based linear FFE was implemented for channel equalization, followed by a two-tap post filter cascaded with the MLSD to suppress the enhanced in-hand noise caused by linear equalization. Finally, BER calculation was performed to evaluate the performance.

Supporting Information

Supporting Information is available from the Wiley Online Library or from the author.

Acknowledgements

The work was supported in part by the National Key R&D Program of China under grant 2023YFB2905503 and the National Natural Science Foundation of China (NSFC) (62035016, 62475146, 62105200, and 62341508). The authors thank the Center for Advanced Electronic Materials and Devices (AEMD) of Shanghai Jiao Tong University (SJTU) for its support in device fabrication.

Conflict of Interest

The authors declare no conflict of interest.

Data Availability Statement

The data that support the findings of this study are available from the corresponding author upon reasonable request.

Keywords

coupled-waveguide devices, robust mode coupling, stimulated raman adiabatic passage, topological photonics

Received: October 21, 2024
Revised: January 7, 2025
Published online: January 31, 2025

[1] Z. Lu, H. Yun, Y. Wang, Z. Chen, F. Zhang, N. A. Jaeger, L. Chrostowski, *Opt. Express* **2015**, *23*, 3795.
[2] D. Dai, J. E. Bowers, *Opt. Express* **2011**, *19*, 10940.
[3] D. Dai, J. Wang, Y. Shi, *Opt. Lett.* **2013**, *38*, 1422.
[4] D. Dai, C. Li, S. Wang, H. Wu, Y. Shi, Z. Wu, S. Gao, T. Dai, H. Yu, H. K. Tsang, *Laser Photonics. Rev.* **2018**, *12*, 1700109.
[5] Y. Huang, G. Xu, S. T. Ho, *IEEE Photonics Technol. Lett.* **2006**, *18*, 2281.
[6] Y. J. Hung, C. H. Chen, G. X. Lu, F. C. Liang, H. C. Chung, S. Y. Tseng, *Opt. Laser Technol.* **2022**, *145*, 107485.
[7] L. Sun, Y. Zhang, Y. He, H. Wang, Y. Su, *Nanophotonics* **2020**, *9*, 1321.
[8] L. Sun, R. Hu, Z. Zhang, Y. He, Y. Su, *IEEE J. Sel. Top. Quantum Electron.* **2021**, *27*, 8100308.
[9] R. Hu, L. Sun, Z. Zhang, Q. Sun, Y. Pan, Y. Su, *Opt. Express* **2023**, *31*, 23542.
[10] W. Song, W. Sun, C. Chen, Q. Song, S. Xiao, S. Zhu, T. Li, *Laser Photonics. Rev.* **2020**, *14*, 1900193.

[11] L. Sun, H. Wang, Y. He, Y. Zhang, G. Tang, X. He, J. Dong, *Laser Photonics. Rev.* **2022**, *16*, 2200354.
[12] U. Gaubatz, P. Rudecki, S. Schiemann, K. Bergmann, *J. Chem. Phys.*, AIP Publishing, Melville, NY, USA **1990**.
[13] N. V. Vitanov, A. A. Rangelov, B. W. Shore, K. Bergmann, *Rev. Mod. Phys.* **2017**, *89*, 015006.
[14] E. Paspalakis, *Opt. Commun.* **2006**, *258*, 30.
[15] S. Longhi, G. D. Valle, M. Ornigotti, P. Laporta, *Phys. Rev. B* **2007**, *76*, 201101.
[16] C. Ciret, V. Coda, A. A. Rangelov, D. N. Neshev, G. Montemezzani, *Phys. Rev. A* **2013**, *87*, 013806.
[17] H. S. Hristova, A. A. Rangelov, G. Montemezzani, N. V. Vitanov, *Phys. Rev. A* **2016**, *93*, 033802.
[18] J. Y. Sie, H. C. Chung, X. Chen, S. Y. Tseng, *Opt. Express* **2019**, *27*, 37622.
[19] R. Alrifai, V. Coda, T. Alhaddad, H. Taleb, A. A. Rangelov, G. Montemezzan, *Phys. Rev. A.* **2023**, *107*, 013527.
[20] W. Song, Y. Chen, H. Li, S. Gao, S. Wu, C. Chen, S. Zhu, T. Li, *Laser Photonics. Rev.* **2021**, *15*, 2000584.
[21] Y. He, X. Li, Y. Zhang, S. An, H. Wang, H. Chen, Y. Huang, N. K. Fontaine, R. Ryf, Y. Du, L. Sun, X. Ji, X. Guo, Y. Song, Q. Zhang, Y. Su, *Adv. Photonics* **2023**, *5*, 056008.
[22] W. Zhao, Y. Peng, X. Cao, S. Zhao, R. Liu, Y. Wei, D. Liu, X. Yi, S. Han, Y. Wan, K. Li, G. Wu, J. Wang, Y. Shi, D. Dai, *Nanophotonics* **2022**, *11*, 4299.
[23] Y. Shen, N. C. Harris, S. Skirlo, M. Prabhu, T. Baehr-Jones, M. Hochberg, X. Sun, S. Zhao, H. Larochelle, D. Englund, M. Soljačić, *Nat. Photonics* **2017**, *11*, 441.
[24] H. Zhang, M. Gu, X. D. Jiang, J. Thompson, H. Cai, S. Paesani, R. Santagati, A. Laing, Y. Zhang, M. H. Yung, Y. Z. Shi, F. K. Muhammad, G. Q. Lo, X. S. Luo, B. Dong, D. L. Kwong, L. C. Kwek, A. Q. Liu, *Nat. Commun.* **2021**, *12*, 457.
[25] L. Feng, M. Zhang, X. Xiong, D. Liu, Y. Cheng, F. Jing, X. Qi, Y. Chen, D. He, G. Guo, G. Guo, D. Dai, X. Ren, *Phys. Rev. Lett.* **2022**, *128*, 060501.
[26] L. Feng, M. Zhang, X. Xiong, Y. Chen, H. Wu, M. Li, G. Guo, G. Guo, D. Dai, X. Ren, *npj Quantum Inf.* **2019**, *5*, 2.
[27] L. Feng, M. Zhang, Z. Zhou, M. Li, X. Xiong, L. Lu, B. Shi, G. Guo, D. Dai, X. Ren, G. Guo, *Nat. Commun.* **2016**, *7*, 11985.
[28] M. Nakahara, *Geometry, Topology and Physics*, Taylor & Francis Group, Abingdon, Oxon, UK **2003**.
[29] W. Liu, C. Li, B. Wang, T. Chai, L. Zheng, Z. Liu, X. Li, C. Zeng, J. Xia, P. Lu, *Laser Photonics. Rev.* **2024**, 2401492. https://onlinelibrary.wiley.com/doi/full/10.1002/lpor.202401492
[30] Y. Su, Y. Zhang, C. Qiu, X. Guo, L. Sun, *Adv. Mater. Technol.* **2020**, *5*, 1901153.
[31] Y. Su, Y. Zhang, *Passive Silicon Photonic Devices: Design, Fabrication, and Testing*, AIP Publishing, Melville, NY, USA **2022**.
[32] X. Zhao, Y. Wang, Q. Huang, J. Xia, *Opt. Express.* **2017**, *25*, 2654.
[33] D. Guo, T. Chu, *Opt. Express.* **2017**, *25*, 9160.
[34] X. Wang, H. Yu, Q. Zhang, Z. Fu, P. Xia, Q. Huang, N. Ning, Z. Wei, Y. Wang, X. Jiang, J. Yang, *Opt. Lett.* **2022**, *47*, 2198.
[35] X. Guo, Y. Liu, J. Du, Q. Song, K. Xu, *J. Light. Technol.* **2022**, *40*, 4682.
[36] H. Xie, Y. Liu, S. Wang, Y. Wang, Y. Yao, Q. Song, J. Du, Z. He, K. Xu, *IEEE. Photonic. Tech. L.* **2020**, *32*, 166.
[37] W. Jiang, J. Hu, S. Mao, H. Zhang, L. Zhou, *J. Light. Technol.* **2021**, *39*, 5042.
[38] H. Shu, B. Shen, Q. Deng, M. Jin, X. Wang, Z. Zhou, *IEEE Photonics. J.* **2019**, *11*, 1.
[39] A. Blanco-Redondo, I. Andonegui, M. J. Collins, G. Harari, Y. Lumer, M. C. Rechtsman, B. J. Eggleton, M. Segev, *Phys. Rev. Lett.* **2016**, *116*, 163901.
[40] G. Tang, X. Chen, L. Sun, C. Guo, M. Li, Z. Tian, H. Chen, H. Wang, Q. Sun, Y. Pan, X. He, Y. Su, J. Dong, *Light Sci. Appl.* **2024**, *13*, 166.
[41] Y. Lahini, F. Pozzi, M. Sorel, R. Morandotti, D. N. Christodoulides, Y. Silberberg, *Phys. Rev. Lett.* **2008**, *101*, 193901.
[42] H. P. Chung, K. H. Huang, S. L. Yang, W. K. Chang, C. W. Wu, F. Setzpfandt, T. Pertsch, D. N. Neshev, Y. H. Chen, *Opt. Express.* **2015**, *23*, 30641.
[43] Y. X. Lin, M. Younesi, H. P. Chung, H. K. Chiu, R. Geiss, Q. H. Tseng, F. Setzpfandt, T. Pertsch, Y. H. Chen, *Opt. Express.* **2021**, *29*, 27362.